A&A 482, 81–95 (2008)
DOI: 10.1051/0004-6361:20078526

Astronomy & Astrophysics

The VIMOS VLT deep survey

The *K*-band follow-up in the 0226-04 field⋆

S. Temporin[1,2], A. Iovino[2], M. Bolzonella[4], H. J. McCracken[11,12], M. Scodeggio[3], B. Garilli[3], D. Bottini[3], V. Le Brun[10], O. Le Fèvre[10], D. Maccagni[3], J. P. Picat[8], R. Scaramella[5,14], L. Tresse[10], G. Vettolani[5], A. Zanichelli[5], C. Adami[10], S. Arnouts[10], S. Bardelli[4], A. Cappi[4], S. Charlot[9,11], P. Ciliegi[4], T. Contini[8], O. Cucciati[2,15], S. Foucaud[22], P. Franzetti[3], I. Gavignaud[13], L. Guzzo[2], O. Ilbert[21], B. Marano[7], C. Marinoni[19], A. Mazure[10], B. Meneux[2,3], R. Merighi[4], S. Paltani[16,17], R. Pellò[8], A. Pollo[10,19], L. Pozzetti[4], M. Radovich[6], D. Vergani[3], G. Zamorani[4], E. Zucca[4], M. Bondi[5], A. Bongiorno[7], J. Brinchmann[20], S. de la Torre[10], F. Lamareille[8], Y. Mellier[11,12], and C. J. Walcher[10]

(Affiliations can be found after the references)

Received 22 August 2007 / Accepted 1 February 2008

ABSTRACT

Aims. We present a new K_s-band survey that represents a significant extension to the previous wide-field K_s-band imaging survey within the 0226-04 field of the VIMOS-VLT deep survey (VVDS). The new data add ∼458 arcmin^2 to the previous imaging program, thus allowing us to cover a total contiguous area of ∼600 arcmin^2 within this field.

Methods. Sources were identified both directly on the final K-band mosaic image and on the corresponding, deep $\chi^2 - g'r'i'$ image from the CFHT Legacy Survey in order to reduce contamination, while ensuring compilation of a truly K-selected catalogue down to the completeness limit of the K_s-band. The newly determined K_s-band magnitudes are used in combination with the ancillary multiwavelength data for determining accurate photometric redshifts.

Results. The final catalogue totals ∼52 000 sources, out of which ∼4400 have a spectroscopic redshift from the VVDS first epoch survey. The catalogue is 90% complete down to $K_{\rm Vega} = 20.5$ mag. We present K_s-band galaxy counts and angular correlation function measurements down to this magnitude limit. Our results are in good agreement with previously published work. We show that using K magnitudes to determine photometric redshifts significantly lowers the incidence of catastrophic errors. The data presented in this paper are publicly available through the CENCOS database.

Key words. infrared: galaxies – galaxies: general – surveys – cosmology: large-scale structure of Universe

1. Introduction

Near-infrared galaxy surveys are widely recognised as giving a number of advantages with respect to optical surveys as tools for studying the process of mass assembly at high redshifts. The observed K-band gives a measure of the rest-frame optical fluxes for intermediate-redshift galaxies up to $z \sim 2$; therefore, it can be more easily related to the galaxy mass in stars. Furthermore, the K-band selection leads to including extremely red objects that would otherwise be missed by a selection in the optical regime. Additional advantages over optical surveys are given by the weaker effects of extinction on K-band observations and by the smaller required k-correction, with little dependence on the galaxy types. Near-infrared data are also particularly useful for more accurately determining photometric redshifts, a key issue especially in the redshift range $1 < z < 2$, where the measurement of spectroscopic redshifts can be challenging.

In fact, in recent years several efforts have been devoted to compiling K-selected samples of galaxies, including spectroscopic surveys of K-selected sources such as the K20 survey (Cimatti et al. 2002). However, surveys reaching very faint K-band magnitudes tend to be limited to rather small sky areas (and thus are affected by cosmic variance; e.g. FIRES, Labbé et al. 2003, down to a depth $K \sim 24$ over a few square arcminutes), while surveys on large areas are often only moderately deep (e.g. Daddi et al. 2000; Drory et al. 2001; Kong et al. 2006, down to $K \sim 19$ over several hundred square arcminutes). A recent overview of the depth and area of published near-IR imaging surveys can be found in Fig. 15 of Förster Schreiber et al. (2006).

Only very recently have surveys started to appear that cover the intermediate regime of area and depth. Some examples are the UKIDSS Ultra Deep Survey and Deep ExtraGalactic Survey (DR1; various levels of depth and coverage over several square degrees, Warren et al. 2007), the MUSYC survey (5σ $K_{\rm Vega} \sim 21$ over 4 fields $10' \times 10'$ each, Quadri et al. 2007), and the Palomar

⋆ Based on observations collected at the European Southern Observatory New Technology Telescope, La Silla, Chile, programme 075.A-0752(A), on data obtained with the European Southern Observatory Very Large Telescope, Paranal, Chile, programme 070.A-9007(A), and on observations obtained with MegaPrime/MegaCam, a joint project of CFHT and CEA/DAPNIA, at the Canada-France-Hawaii Telescope (CFHT), which is operated by the National Research Council (NRC) of Canada, the Institut National des Science de l'Univers of the Centre National de la Recherche Scientifique (CNRS) of France, and the University of Hawaii. This work is based in part on data products produced at TERAPIX and the Canadian Astronomy Data Centre as part of the Canada-France-Hawaii Telescope Legacy Survey, a collaborative project of NRC and CNRS.

Observatory Wide-Field Infrared Survey (1.53 deg^2 over 4 fields, down to $K_{\rm Vega} \sim 20.5$, Conselice et al. 2007).

Here we present a new K-band survey that, in the context of the VIMOS-VLT deep survey (VVDS Le Fèvre et al. 2005), significantly enlarges the area already surveyed by Iovino et al. (2005), although to a shallower depth, thus yielding a wide K-band contiguous field of ∼629 arcmin^2 within the 0226-04 VVDS field (F02). This dataset benefits from the multiwavelength information already available for the field F02, namely optical and ultraviolet imagery available through the VVDS ($UBVRI$; McCracken et al. 2003; Radovich et al. 2004) and the CFHT Legacy Survey ($u^*g'r'i'z'$), J-band imagery available for a sub-area of ∼161 arcmin^2 (Iovino et al. 2005) and, in the radio regime, 2.4 GHz VLA and 610 MHz GMRT data (Bondi et al. 2003, 2007). Spectroscopic observations from the first epoch VVDS (Le Fèvre et al. 2005) targeted 2823 sources from our K-band catalogue to $K_{\rm Vega} \leq 20.5$. Limiting magnitudes (intended as 50% completeness limits) for the available multi-wavelength imagery are: $u^*_{\rm AB} \sim 26.5$, $g'_{\rm AB} \sim 26.4$, $r'_{\rm AB} \sim 26.1$, $i'_{\rm AB} \sim 25.9$, $z'_{\rm AB} \sim 25.0$ (Ilbert et al. 2006); $U_{\rm AB} \sim 25.3$ (Radovich et al. 2004), $B_{\rm AB} \sim 26.5$, $V_{\rm AB} \sim 26.2$, $R_{\rm AB} \sim 25.9$, $I_{\rm AB} \sim 25.0$ (McCracken et al. 2003); $J_{\rm AB} \sim 24.1$ (Iovino et al. 2005).

The primary aim of this paper is to describe in detail the preparation of our K-band catalogue and to quantify its reliability and completeness. While the data reduction described in the following concerns only the newly obtained, shallower K-band data, analysis of the properties is carried out on the entire K-band catalogue, which includes the deep part of the survey already presented by Iovino et al. (2005) and can be considered complete down to $K_{\rm Vega} \leq 20.5$, as shown below. Down to this magnitude, the deep part of the survey makes up 26% of the catalogue.

The photometric sample and the spectroscopic sub-sample whose general properties are described in this paper are then used in a companion paper for the selection and analysis of samples of objects with extreme colours (Temporin et al. 2008). The K-band data described here and in Iovino et al. (2005) have significantly contributed to improving the determination of the galaxy stellar mass function from the VVDS survey, especially for redshifts $z > 1.2$ (up to $z = 2.5$) and for the low-mass tail of the function at lower redshifts, $z < 0.4$ (Pozzetti et al. 2007). Additionally, this K-band catalogue is well-suited to following the evolution of the rest-frame I-band galaxy luminosity function (Bolzonella et al. 2008). The K-band photometry presented in this paper has been made available to the astronomical community through the CENCOS database (Le Brun et al. 2007) at the URL `http://cencosw.oamp.fr/`, from where it can be retrieved, together with the photometry in all other available bands (i.e. VVDS photometry in UBVRI(J) and CFHTLS photometry in $u^*g'r'i'z'$.). The K-band catalogue we present here can be easily obtained by querying the database with the appropriate K magnitude limits.

2. Observations and data reduction

New ancillary data to the VVDS 0226-04 field (hereafter F02) were obtained in the $K_{\rm s}$ filter with the SOFI Near Infrared Imaging camera (Moorwood et al. 1998) at the ESO New Technology Telescope in September 2005 and February 2006. These observations cover the region of sky immediately adjacent to that previously targeted by deep J and $K_{\rm s}$ observations (Iovino et al. 2005), with some overlap on the western and southern sides. Hereafter, we refer to the $K_{\rm s}$-band simply as K-band. The observations were done in a series of pointings in a raster

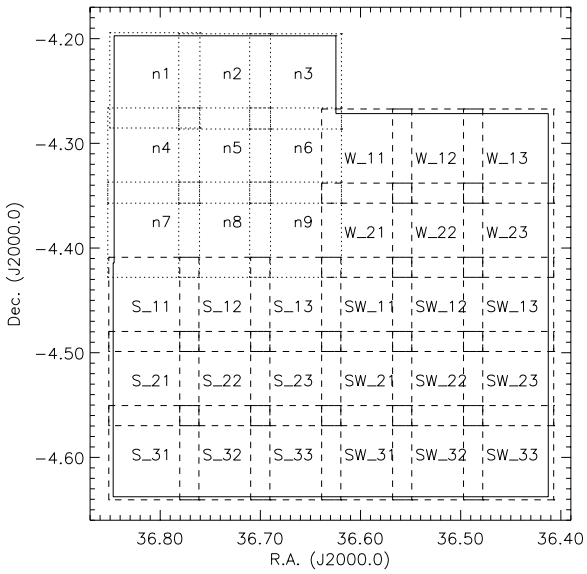

Fig. 1. Sky coverage of the K-band survey. Dotted lines outline the pointings n1 to n9 of the deep survey (Iovino et al. 2005). Dashed lines outline the 24 pointings in the newly surveyed area, labelled as in Table 1. The solid line indicates the final mosaicked area after excision of the borders.

configuration, organised in such a way as to ensure significant overlap between adjacent pointings as illustrated in Fig. 1, in analogy to the observation scheme described in Iovino et al. (2005). A total of 24 fields ∼5′ × 5′ in size, with overlapping borders, have been observed with a series of jittered 90 s exposures, each obtained with a detector integration time DIT = 10 s, and a number of such integrations NDIT = 9. Jittering was performed by randomly offsetting the telescope within a 30″ × 30″ box for a total typical exposure time of 1 h per pointing (except for one field that was exposed for 1.7 h) with an average seeing of ∼1.″1 and a pixel scale of 0.288 arcsec pixel^{-1} (see Table 1 for a list of the pointings and the seeing conditions during the observations). The airmass of the data ranges from 1.11 to 1.38, except for part of one pointing that was observed in February 2006 at an airmass ∼1.6.

After excision of the low signal-to-noise borders and of the regions around bright stars (or very nearby extended galaxies), the new K-band images resulted in a newly covered area of 458.2 arcmin^2 and, when combined with the previous, deeper observations presented in Iovino et al. (2005), in a total K-band area of 623 arcmin^2 within F02. Hereafter, we refer to the combined deep and shallow K-band images as the K-wide image.

Photometric standard stars from Persson et al. (1998) were observed 5 to 9 times per night. Each standard star was centred within each quadrant and near the center of the detector array through a pre-defined sequence of 5 pointings (DIT = 1.2 s, NDIT = 15 each).

2.1. Data reduction

The data reduction procedure was largely similar to the one explained in Iovino et al. (2005). The individual frames were corrected for dark current, flat-fielded, and examined for quality assessment by use of IRAF[1] packages and scripts. The

[1] IRAF is distributed by the National Optical Astronomy Observatories, which are operated by the Association of Universities for Research in Astronomy, Inc., under cooperative agreement with the National Science Foundation.

Table 1. Field F02: observations summary.

Pointing	RA h m s	Dec ° ′ ″	Obs date	Coadded frames	t_{exp} (min)	Seeing (arcsec)	Correction term[a] (mag)
S_11	02 27 14	–04 27 03	6 Sept. 05	40	60	1.11 ± 0.14	0.032 ± 0.014
S_12	02 26 57	–04 27 03	5 Sept. 05	40	60	0.67 ± 0.09	0.032 ± 0.015
S_13	02 26 40	–04 27 03	6 Sept. 05	40	60	0.69 ± 0.09	0.032 ± 0.025
S_21	02 27 14	–04 31 18	5 Sept. 05	40	60	1.09 ± 0.14	...
S_22	02 26 57	–04 31 18	5 Sept. 05	7	10.5	1.11 ± 0.10	...
S_22	02 26 57	–04 31 18	5 Feb. 06	30	45	1.03 ± 0.10	0.050 ± 0.035
S_22	02 26 57	–04 31 18	6 Feb. 06	31	46.5	0.96 ± 0.08	0.050 ± 0.035
S_23	02 26 40	–04 31 18	6 Sept. 05	40	60	0.79 ± 0.13	...0
S_31	02 27 14	–04 35 33	4 Sept. 05	40	60	0.99 ± 0.14	0.175 ± 0.055
S_31	02 27 14	–04 35 33	7 Sept. 05	10	15	0.88 ± 0.06	...
S_32	02 26 57	–04 35 33	4 Sept. 05	39	58.5	1.01 ± 0.12	0.014 ± 0.010
S_33	02 26 40	–04 35 33	4 Sept. 05	40	60	0.94 ± 0.07	...
SW_11	02 26 23	–04 27 03	7 Sept. 05	41	61.5	0.88 ± 0.09	...
SW_12	02 26 06	–04 27 03	9 Sept. 05	40	60	1.09 ± 0.05	...
SW_12	02 26 06	–04 27 03	12 Sept. 05	10	15	0.91 ± 0.15	...
SW_13	02 25 49	–04 27 03	11 Sept. 05	20	30	1.09 ± 0.01	...
SW_13	02 25 49	–04 27 03	12 Sept. 05	30	45	1.14 ± 0.18	...
SW_21	02 26 23	–04 31 18	7 Sept. 05	40	60	1.19 ± 0.09	...
SW_22	02 26 06	–04 31 18	8 Sept. 05	40	60	1.05 ± 0.15	0.078 ± 0.021
SW_23	02 25 49	–04 31 18	12 Sept. 05	21	31.5	1.15 ± 0.16	–0.142 ± 0.027
SW_23	02 25 49	–04 31 18	12 Sept. 05	19	28.5	1.06 ± 0.02	0.078 ± 0.017
SW_31	02 26 23	–04 35 33	7 Sept. 05	39	58.5	0.81 ± 0.08	...
SW_32	02 26 06	–04 35 33	8 Sept. 05	39	58.5	0.85 ± 0.05	0.102 ± 0.021
SW_33	02 25 49	–04 35 33	12 Sept. 05	34	51	0.94 ± 0.10	...
SW_33	02 25 49	–04 35 33	9 Sept. 05	10	15	1.05 ± 0.05	...
W_11	02 26 23	–04 18 33	6 Sept. 05	20	30	0.85 ± 0.14	–0.095 ± 0.020
W_11	02 26 23	–04 18 33	8 Sept. 05	20	30	1.52 ± 0.15	–0.116 ± 0.035
W_12	02 26 06	–04 18 33	9 Sept. 05	40	60	1.40 ± 0.10	–0.116 ± 0.035
W_12	02 26 06	–04 18 33	12 Sept. 05	10	15	0.92 ± 0.10	–0.134 ± 0.040
W_13	02 25 49	–04 18 33	11 Sept. 05	40	60	1.21 ± 0.10	–0.116 ± 0.035
W_13	02 25 49	–04 18 33	12 Sept. 05	10	15	1.10 ± 0.15	–0.179 ± 0.048
W_21	02 26 23	–04 22 48	8 Sept. 05	40	60	1.16 ± 0.12	–0.047 ± 0.020
W_22	02 26 06	–04 22 48	9 Sept. 05	40	60	1.19 ± 0.07	–0.078 ± 0.022
W_22	02 26 06	–04 22 48	12 Sept. 05	10	15	1.18 ± 0.07	–0.190 ± 0.040
W_23	02 25 49	–04 22 48	11 Sept. 05	40	60	1.08 ± 0.12	–0.073 ± 0.049

[a] Photometric correction terms that have been applied to bring the photometry into agreement with the reference field SW_21.

quality check involved the evaluation of fluctuations of the sky-background and of the magnitude and the *FWHM* of a reference star along each exposure sequence, as well as a check for the presence of any artifacts that could compromise the quality of the final coadded image. Low-quality images, or images whose seeing was significantly worse compared to that of the other images in the same sequence, were discarded. The final total exposure times and the number of useful frames per pointing and observing date, after excluding lower quality frames, are listed in Table 1, where the individual pointings are named according to the scheme of Fig. 1. The average seeing as measured on the final coadded images and the photometric correction terms (see below) applied to each field are reported, too.

The IRDR stand-alone software (Sabbey et al. 2001) was used for the sky-background subtraction, the coaddition of the images that composed each exposure sequence, and the construction of the associated weight maps. When the exposure sequence of a given pointing was split between two different nights, two separate coadded images were built, one per night of observation. Exposure sequences were also split during the coaddition phase in the case of a sudden change in the sky conditions during the observations (e.g. changed background-sky level and/or seeing).

The reduction of the photometric standard stars proceeded in a similar way, including the quality assessment of the individual frames. A photometric zero-point was determined for each night of observation by measuring the aperture magnitudes of the standard stars observed during the same night and comparing them with published magnitudes. Uncertainties in the zero-points are 0.01−0.02 mag, depending on the night of observation, for the 2005 September run, and 0.03 mag for the two observing nights of 2006 February. As a value for the atmospheric extinction coefficient, we adopted the one available from the European Southern Observatory web site for the nearest dates to our observations[2]. Thus, the values we used are 0.05 for the 2005 observations and 0.03 for the observations of 2006 February.

The coadded images of F02 were transformed to flux values above the atmosphere and calibrated with the zero-points according to the values that were obtained during the nights of observation. Finally the images were rescaled to an arbitrary common zero-point and transcribed to the *AB* magnitude system with zero point 30.0. Since not all our nights offered excellent photometric quality, some refinement of the photometric calibration was necessary. To ensure homogeneous calibration across the final mosaicked image, the measured magnitudes of the stars in the overlapping regions of adjacent pointings and in multiple, coadded images of the same pointing (obtained either in

[2] See SOFI web page: `www.ls.eso.org/lasilla/sciops/ntt/sofi/index.html`

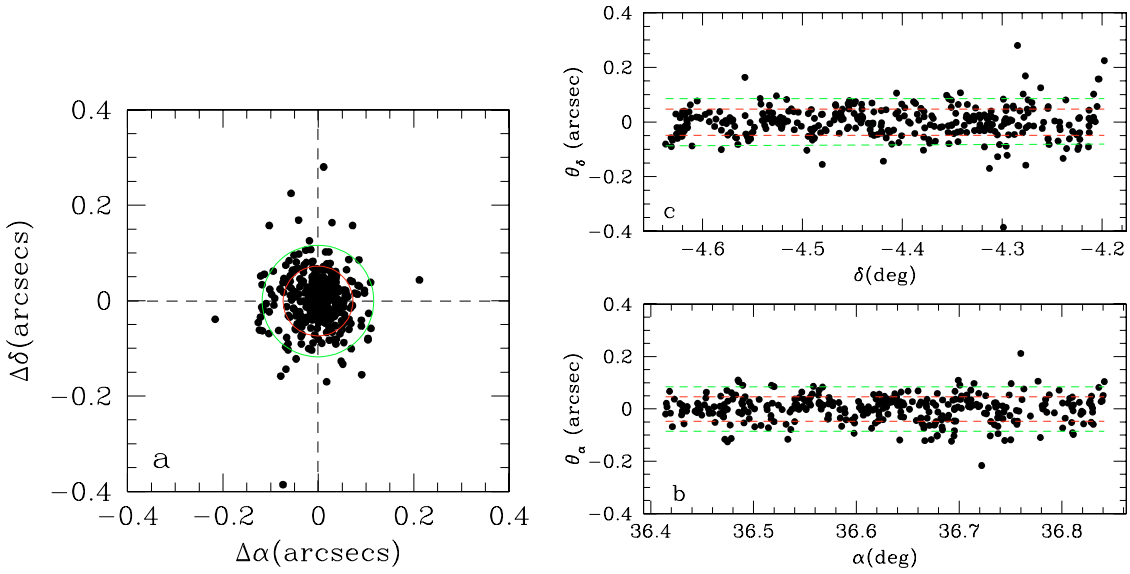

Fig. 2. Radial (a), right-ascension (b), and declination (c) residuals between the K-band and i'-band positions for unsaturated, point-like sources. The inner (red) and outer (green) dashed circles/lines enclose 68% and 90% of all objects, respectively. The centroid of the distribution of radial residuals is indicated by crossed dashed lines.

different nights or with different sky conditions) were used to test the photometric calibration and to determine the flux scale factors to be applied to the individual coadded images, when necessary. For this purpose, we took as reference for the photometry the pointing that was observed under the best conditions during the observing run, as it emerged from our quality checks. This was the pointing SW_21. The zero-point uncertainty for the night of observation of SW_21 is 0.01 mag. Scaling factors were ignored both in the case of very small corrections (<0.01 mag) and in the case of errors in determining the scale factor larger than the correction itself. No scaling factor was applied to 14 out of 35 coadded frames. The correction terms applied to the remaining frames are in the range 0.01−0.18 mag, with a median value of 0.08 mag; the individual values with their uncertainties are given in Table 1. Finally, after applying these scale factors, the stars in the overlapping regions between the new K-band observations and the previous deep observations were used to check the consistency of the absolute photometric calibration with what was obtained for the deep-K survey. No systematic shift was detected in the photometric calibration.

The astrometric calibration of the coadded images was a two-step process. A first-order astrometric solution was found by taking the astrometric catalogue of the United States Naval Observatory (USNO)-A2.0 (Monet 1998) as reference, then the solution was refined by using as reference the position of non-saturated point-like sources in the astrometrised CFHTLS i'-band image of the field. This procedure, already applied to the deep-K (Iovino et al. 2005), BVR (McCracken et al. 2003), and U (Radovich et al. 2004) images, allowed us to reach a higher relative astrometric accuracy and to match sources at the sub-pixel level between optical and K bands. The rms of these astrometric solutions ranges between 0.″056 and 0.″123, with a median value of 0.″099. The astrometrised and photometrically calibrated images of the individual pointings, weighted by the relevant weight maps, were combined in a mosaic, together with the deep K-band images and, at the same time, regridded to a final pixel scale of 0.186 arcsec pixel^{-1}, to match the scale of the CFHTLS optical images. During this operation, performed with the software SWarp[3] (Bertin et al. 2002), the relevant flux scale factors, determined as explained above, were applied to the individual coadded images to put the photometry of the final mosaic on a homogeneous basis. A similarly constructed mosaic of the weight maps was obtained for use in the source detection phase. See McCracken et al. (2003) for further details on the stacking procedure with SWarp. The median seeing measured on the K-wide image as the $FWHM$ of non-saturated point-like sources is ∼1.″0.

2.1.1. Quality of astrometric calibration

A catalogue of CFHTLS i'-band point-like sources was used to verify the goodness of the astrometric calibration of the final K-band mosaic. We ran SExtractor (Bertin & Arnouts 1996) on the image as a detection algorithm. A representation of the radial offsets of K-detected stars with respect to their catalogued positions is shown in Fig. 2. No systematic offset was detected either in right ascension or in declination. The measured positions agree with the catalogued ones within 0.″07 (0.″12) for 68% (90%) of the sources. A separate examination of the residuals between K-band and i'-band positions as a function of right ascension and declination (Fig. 2) does not show any dependence on the location in the frame. The quality of the astrometric calibration is uniform throughout the final mosaicked image. The K-band positions agree with the i'-band ones within 0.″047 (0.″086) for 68% (90%) of the point-like sources in both right ascension and declination.

2.1.2. Quality of photometry

The quality checks on the image sequences of the target and standard star fields described above, and the comparison of the magnitudes between the deep and the shallow parts of our K-band survey have already indicated the reliability of our photometry.

[3] Software developped by E. Bertin and available at the URL http://terapix.iap.fr

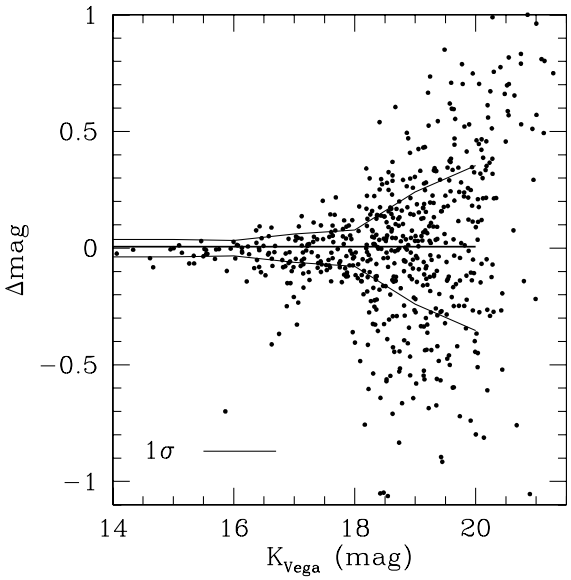

Fig. 3. Photometric error as a function of the K-band magnitude obtained as a comparison of the magnitudes from two 30-min exposures of the same field. The thick solid line indicates the mean magnitude difference between the two images and the thin solid lines indicate the 1σ error as a function of the $K_{\rm Vega}$ magnitude. The typical 1σ error in the magnitudes of the final stacked 1hr exposure will be half of the error reported in this plot.

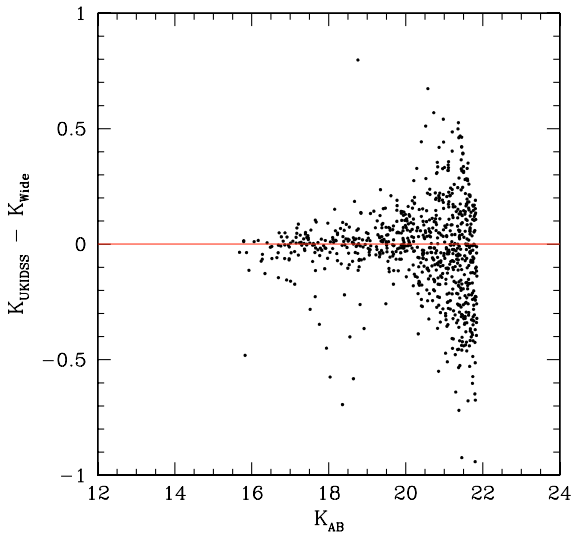

Fig. 4. Comparison of our photometry with the K-band photometry from the early data release of the UKIDSS survey (Dye et al. 2006). Only point-like sources with a 10σ detection were considered. The solid line indicates the mean value of the magnitude difference.

The photometric errors as a function of the K magnitude were estimated by using repeated exposures on the same region of the sky. The source detection was performed with SExtractor and the MAG_AUTO parameter from the output file was adopted as a measure of the total magnitudes. An example is shown in Fig. 3, where two 30-min exposures were used for the comparison. Since both images contribute equally and independently to the measured error σ shown in Fig. 3, the uncertainty for an individual 30 min exposure is given by $\sigma/\sqrt{2}$. Then, coadding the two images to obtain the final stacked image (we recall that the typical exposure time for the stacked image is 1 h) reduces the individual errors by a further factor $1/\sqrt{2}$. Hence, the final error will be a half of the value measured with the above comparison. Therefore, for the final stacked image of a pointing, the estimated 1σ errors are 0.04, 0.12, and 0.17 mag at $K_{\rm Vega}$ = 18, 19, and 20 mag, respectively.

As an independent check of the goodness of our photometry, we compared our K-band magnitudes with those from the UKIDSS Early Data Release (Dye et al. 2006) in F02 (Deep Extragalactic Survey, DXS, see Fig. 14 of Dye et al. (2006) for an indication of coverage and depth) and found them to be in reasonable agreement, although with some spread. No significant systematic offset is present. In Fig. 4 we show the comparison for all cross-identified, bona-fide point-like sources that were selected for having a SExtractor FLUX_RADIUS parameter $r_{1/2} > 2.7$ in the i'-band (see Ilbert et al. 2006) and have $K_{\rm Vega} < 20$ in our catalogue, roughly corresponding to a $>10\sigma$ detection on our K-band image.

3. The *K*-band catalogue

3.1. Building the catalogue

The construction of the catalogue went through a series of steps aimed at obtaining a catalogue as complete as possible in the K-band – suited to the extraction of K-selected galaxy samples – while minimising the incidence of spurious detections without affecting our completeness. This goal was achieved by matching the results of two detection procedures, one performed directly on the K-band image, and the other based on the use of a χ^2 image, constructed using the technique outlined in Szalay et al. (1999). The latter had the main purpose of pruning spurious detections from the catalogue, especially in the K-faint regime and obtaining K-band magnitudes already matched with the optical ones, which were obtained starting from the same χ^2 detection image (see also McCracken et al. 2003; Radovich et al. 2004, for the use of χ^2 images in the preparation of VVDS photometric catalogues in other wavelengths).

The steps we followed are given below. The detection and measurement of the sources on the final mosaicked image with the associated weight map were obtained with SExtractor by applying similar criteria to those described in Iovino et al. (2005). As a measure of total magnitudes in our catalogue, we used the SExtractor parameter MAG_AUTO.

Step 1. A $\chi^2 - g'r'i'$ image built from CFHTLS data was used as the detection image to measure the K-band sources with SExtractor in double-image mode. The use of the χ^2 image has the advantage of reducing the number of spurious detections, while still picking up most of the reliable sources that are present in our K-band image. The χ^2 image and the K-wide image have sufficiently similar seeing to assure the effectiveness of this procedure. For an object to be included in our catalogue, it must contain at least three contiguous pixels above a per-pixel detection threshold of 0.4σ in the χ^2 image. This step produced the version 1 (V1) of our catalogue and offered us a direct cross-identification of the K-band sources with those listed in the CFHTLS catalogue for the same region of the sky (Ilbert et al. 2006).

Step 2. A second version of the catalogue (V2) was produced by using SExtractor in single-image mode (i.e. without a separated detection image) on the K-wide image. This was a key step in the creation of a K-selected catalogue, and it was necessary to ensure that we would not miss any real K-band source that escaped detection in the χ^2 image. In this case, to reduce the number of fake detections, we chose to include in the catalogue the

objects containing at least 9 contiguous pixels above a per-pixel detection threshold of 1.1σ.

Step 3. A positional match of sources between the two catalogues was obtained by adopting 1.″0 as an upper limit to the separation for a source to be considered the same. Tests with different upper limits to the source separation showed that our choice was conservative enough to include all sources present in both catalogues and sufficiently small to minimise false matches. This procedure provided us with a list of objects that were detected in the K-wide image but were not in the χ^2 image. Besides truly red objects, this list included members of (apparent) pairs that are resolved in the K-band image but appear as an individual source in the χ^2 image (see Step 6 below), sources that fall in the vicinity of bright objects and are, therefore, masked by bright halos in the χ^2 image, and, finally, a number of fake detections that needed to be expunged.

Step 4. To refine the object list produced at Step 3, we evaluated the level of contamination from fake detections as a function of magnitude. To this purpose we applied SExtractor to the inverse of the K-wide image, with the same parameters we used for the production of the catalogue V2. The contamination level within 0.5 mag bins was estimated as the fraction of detections in the inverse image with respect to the original image. The resulting contamination rate is 9% in the bin centred at $K_{\rm Vega}$ = 19.75 and reaches 23% in the bin centred at $K_{\rm Vega}$ = 20 (i.e. in the range 19.75−20.25 mag). We note that this contamination rate is relevant for the sources that were detected using only the K-band image, while it is not representative of the contamination from spurious detections of catalogue V1, for which the effect is minimised by the use of the χ^2 image (as demonstrated in Iovino et al. 2005).

To limit the amount of contamination, out of all K-band detections for which it was impossible to identify a counterpart in the catalogue V1, we selected those with a magnitude $K_{\rm Vega} \leq$ 20.25 and, out of these, we retained only those sources that appeared reliable upon visual inspection of the K-band and optical images. These remaining 726 sources were added to catalogue V1. Their magnitudes in the other available bands were determined by running SExtractor on the relevant optical images by using the K-band as the detection image.

Step 5. A positional match of our K-band detections (catalogue V2) with catalogued VVDS sources in the relevant region of the sky, allowed us to ensure the inclusion in our catalogue of all objects with a measured spectroscopic redshift. At this step we added to our catalogue another 66 K-detected sources. These sources did not have a counterpart in the catalogue V1 because of their proximity to bright stars in the χ^2 image. Also, they were missed by our Step 4 because most of them are fainter than the threshold $K_{\rm Vega}$ = 20.25 we adopted for including additional sources from catalogue V2. In fact they are $\gtrsim 3\sigma$ detections with an average magnitude $K_{\rm Vega} \sim 20.9$, 13 of them having $K_{\rm Vega} < 20.5$.

Step 6. A comparison of the magnitudes of the sources in common between the catalogues V1 and V2 showed generally good agreement, thus indicating that the additional sources identified in catalogue V2 could be safely added to the main catalogue without need of aperture corrections. However, a number of sources showed a remarkable magnitude difference between the two catalogues and required further investigation. We adopted as a criterion for selecting sources with deviant magnitudes the simultaneous satisfaction of the conditions: $|K_{\rm Vega\_V1} - K_{\rm Vega\_V2}| > 5\sigma$ (where σ was obtained by adding in quadrature the errors on the individual magnitudes) and $|K_{\rm Vega\_V1} - K_{\rm Vega\_V2}| > 0.2$ (to exclude the cases with small absolute deviations but with very small magnitude errors, which would be selected by our first condition). The search was limited to objects brighter than $K_{\rm Vega}$ = 20.25, in analogy to Step 4.

About 300 objects were selected this way and visually inspected to check for correct cross-identification between the two catalogues and for possible problems. These objects were found to include false matches, matches with K-band false detections, source blends that had been correctly deblended only in the K-band image but not in the χ^2 image, and vice-versa, source blends that had been correctly deblended in the χ^2-image but remained unresolved as an individual source in the K-band image. We corrected the catalogue for the relevant cases by rejecting false detections and adopting magnitude measurements based on the K-band image instead of the χ^2-image for blends that were unresolved in the latter. In contrast, for blends that were unresolved in the K-band but correctly resolved in the χ^2-image, we kept the identifications and magnitudes of catalogue V1. In both cases, that these sources were actually blends of multiple sources and not multiple clumps within a single galaxy appeared obvious from the visual inspection of the individual optical and near-infrared images.

Step 7. For the deep area of the survey, a comparison between the magnitudes obtained using the new χ^2 image and those presented in Iovino et al. (2005), based on a $\chi^2 - BVRIK$ image, did not reveal any systematic difference and showed that the new measurements are equivalent (within the errors) to the original ones. Therefore, for consistency with the previously published paper, in our final catalogue we adopted the original magnitudes for the deep part of the survey.

Step 8. A correction for Galactic extinction on an object-by-object basis was applied to the magnitudes in the final catalogue by using Schlegel et al. (1998) dust maps.

3.2. Completeness

An indicative estimate of the limiting magnitude of our survey can be simply obtained based on the background rms of the coadded images and on the seeing during the observations. The $n\sigma$ magnitude limits are given by $\mathrm{mag}(n\sigma) = zp - 2.5\log(n\sigma\sqrt{A})$, where zp is the zero point and A the area of an aperture whose radius is the average *FWHM* of unsaturated point-like sources (see Table 1). The values estimated this way for n = 3, 5 are $\mathrm{mag}(3\sigma) \sim 21.4$ and $\mathrm{mag}(5\sigma) \sim 20.9$ (in the Vega system). Indeed, by measuring the signal-to-noise ratio as a function of K-band magnitude across the final K-wide image in a 3.′1-wide running box with a step of 37″ (i.e. 200 pixels) (and by imposing the relevant positional constraints to keep the box within the borders of the K-wide image as marked with a solid line in Fig. 1), we obtained a magnitude limit for 3σ detections that varies in the range $K_{\rm Vega}$ = 21.4−22.8, the brightest limit being referred to the shallower part of the image, which is the subject of the present paper.

However, a better characterisation of the photometric properties of our final image is given by the estimate of the completeness level in the source detection at various magnitudes. We determined the completeness level from our ability to recover artificial point-like sources inserted at random positions in our image. The detection of artificial sources was performed with the same SExtractor parameters as were adopted for the real sources. The procedure we followed does not differ from that adopted by Iovino et al. (2005) so we refer the reader to that paper for further details. A representation of the completeness level as a function of magnitude for the shallow part of our K-band survey is shown

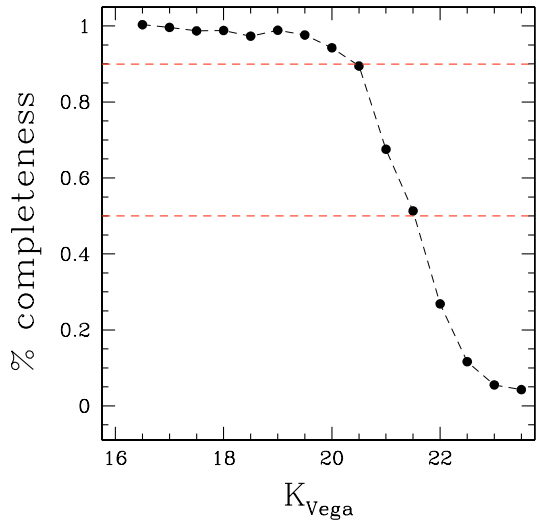

Fig. 5. Completeness level of our K-shallow survey as a function of magnitude. The 50% and 90% completeness levels are marked with dashed lines.

in Fig. 5. In particular we reach a nominal completeness level of 90% (50%) for point-like sources with $K_{\rm Vega} \leq 20.5$ (21.5). The completeness level for the deep part of the survey (as estimated in Iovino et al. 2005) is 90% (50%) to $K_{\rm Vega} \leq 20.75$ (22.00).

However, the determination of the actual completeness of our final catalogue is more complex than described above. In fact, while the completeness test was run on the K-band image alone, the use of the χ^2-image played a role in the completeness level that was finally achieved. On the other hand, having used the χ^2-image to detect sources, there is a concern that our catalogue is not a purely K-selected one, at least for the shallow part of the survey that is the object of this paper. As explained in the previous section, for $K_{\rm Vega} \leq 20.25$, all sources with a significant detection in the K-band image have been included. Furthermore, for $K_{\rm Vega} \leq 20.50$ the depth of the images composing the χ^2-image implies that the last is fully sufficient to recover sources even with the reddest colours while, at the same time, reducing the number of spurious detections. Therefore, our conclusion is that, down to $K_{\rm Vega} = 20.5$ where we reach a nominal completeness level of 90% for point-like sources, we can safely state that our catalogue is a truly K-selected one. The achieved completeness level is supported by the raw number counts (see Sect. 6) that do not fall below a power law, at least up to $K_{\rm Vega} = 20.5$.

The remaining potential problems for the $K_{\rm Vega} > 20.5$ regime are i) possible cases of association of χ^2-detected sources with correlated noise in the K-band image; and ii) some possible level of colour incompleteness that could arise from missing extremely red, K-faint sources that could have remained undetected in the χ^2 image. Therefore, for such faint magnitude regimes we cannot state that our catalogue is a purely K-selected one, having nevertheless been designed to be as complete as possible in both the optical and in K-band. This caveat should be kept in mind when in the next sections we refer to our catalogue as a K-selected one: this attribute is, strictly speaking, correct only for $K_{\rm Vega} < 20.5$.

3.3. The K-wide photometric sample

Our final K-wide catalogue totals 51 959 detections. It contains 22 846 objects down to our limiting magnitude (i.e. 50% completeness limit) $K_{\rm Vega} \leq 21.5$ and 10 615 objects down to our 90% completeness limit[4] $K_{\rm Vega} \leq 20.5$.

However, to be sure we are dealing with a truly K-selected catalogue and to avoid contamination by spurious sources, for future analysis we restrict our final photometric sample to the 8856 objects down to $K_{\rm Vega} \leq 20.25$. The number of catalogued objects for different magnitude limits are reported in Table 2 for ease of comparison with other existing surveys. At this level, no distinction has been made between stars and galaxies. This issue is addressed later on in Sect. 5. The magnitude distribution of the sample is shown in Fig. 6. The photometric redshifts for this sample, determined by including the K-band information, are presented in Sect. 4.

Table 2. Field F02: K-selected photometric sample.

$K^a \leq 19.0$	$K \leq 19.5$	$K \leq 19.75$	$K \leq 20.0$	$K \leq 20.25$	$K \leq 20.5$
3608	5152	6180	6399	8857	10 615

[a] All K magnitudes are expressed in the Vega system. Magnitudes in the AB system can be obtained by adding +1.84.

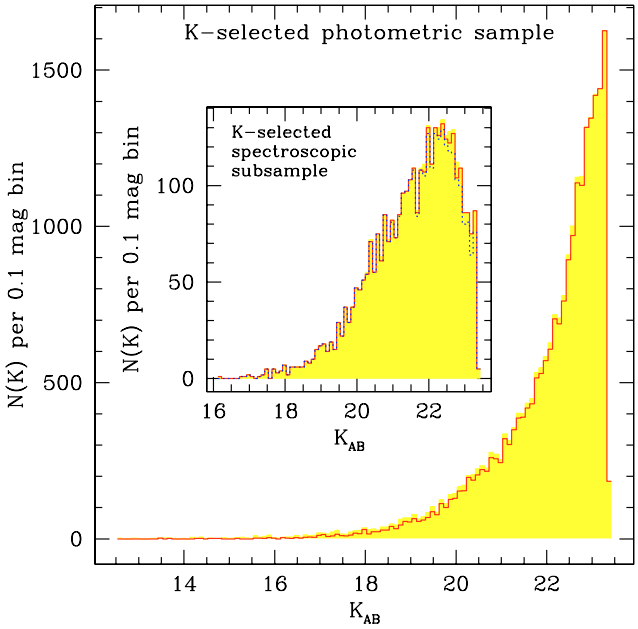

Fig. 6. Magnitude distribution of our K-wide photometric sample down to the magnitude limit of the survey $K_{\rm Vega} \leq 21.5$ for all objects (yellow filled histogram) and for objects classified as galaxies (red histogram; Sect. 5). The inset shows the K-magnitude distribution for the whole K-selected spectroscopic sample (yellow filled histogram), for the objects classified as galaxies within it (red histogram; Sect. 5), and for the galaxy subsample with $17.5 \leq I_{\rm AB} \leq 24.0$ (dotted blue histogram).

3.4. The K-selected spectroscopic sample

Our shallow K-band survey and part of the deep one (i.e. all pointings in Fig. 1 except for n1, n2, and n3) are located in the four-pass area of the VVDS, which implies a spectroscopic sampling rate up to ~40% down to $I_{\rm AB} \leq 24$ (Le Fèvre et al. 2005). Our K-wide catalogue (down to the magnitude limit of the survey, intended as the 50% completeness limit) contains a total of 4059 objects covered by spectroscopic observations, out of

[4] Hereafter we refer to the 90% and 50% limits as the "completeness limit" and the "limiting magnitude" of our survey.

Table 3. Field F02: number of galaxies/stars in the K-selected spectroscopic sample.

Flags[a]	$K^b \leq 19.0$	$K \leq 19.5$	$K \leq 19.75$	$K \leq 19.8$	$K \leq 20.0$	$K \leq 20.25$	$K \leq 20.5$	$K \leq 21.5$
any	893 / 176	1303 / 201	1566 / 219	1613 / 222	1810 / 239	2113 / 250	2426 / 265	3489 / 325
1, 21	71 / 7	126 / 11	167 / 12	173 / 12	199 / 14	251 / 14	312 / 15	534 / 27
2, 22	183 / 11	304 / 13	385 / 14	394 / 15	456 / 20	551 / 23	656 / 27	1022 / 52
3, 4, 23, 24	613 / 158	834 / 177	968 / 193	999 / 195	1097 / 205	1241 / 213	1375 / 223	1791 / 246
9, 29	7 / 0	13 / 0	18 / 0	18 / 0	25 / 0	36 / 0	48 / 0	105/
11, 211, 12, 212	0 / 0	0 /0	0 / 0	0 / 0	3 / 0	3 / 0	2 / 0	2 / 0
13, 14, 213, 214	16 / 0	21 / 0	22 / 0	22 / 0	22 / 0	23 / 0	25 / 0	26 / 0
19, 219	3 / 0	5 / 0	6 / 0	7 / 0	7 / 0	8 / 0	8 / 0	9 / 0

[a] Flags indicate the spectral quality and reliability of redshift measurements according to the definitions in Le Fèvre et al. (2005).
[b] All K magnitudes are expressed in the Vega system. Magnitudes in the AB system can be obtained by adding +1.84. In this table the star/galaxy separation is based on a purely spectroscopic classification.

which 3815 have a successful measure of redshift (81 of them are secondary objects with $I_{AB} > 24$). The actual spectroscopic sampling rate for the K-wide catalogue down to its 90% completeness limit is 26.6% (27.9% to $K_{Vega} \leq 20.25$), while the success rate is ~95.5% down to the same magnitude limit. Secure (flags 2−4 Le Fèvre et al. 2005) spectroscopic redshifts are available for 1792 galaxies and 23 active galactic nuclei (AGN) down to $K_{Vega} \leq 20.25$ (12 of these objects have $I_{AB} > 24$). The number of galaxies and stars in the sample within various magnitude limits and for various levels of spectral quality is summarised in Table 3. The star-galaxy separation for the spectroscopic sample relies on the spectral classification.

The normalised redshift distribution of our K-selected spectroscopic sample down to the magnitude limits $K_{Vega} \leq 20.25$, 20.50 is shown in Fig. 7 in comparison with the redshift distribution of the whole VVDS sample within the same region of the sky. The distribution is presented both for the case of secure redshifts and for all measured redshifts. We distinguish the case in which all available redshifts are considered, irrespective of the I-band magnitudes, and the case where only objects within the magnitude limits of the spectroscopic survey ($17.5 \leq I_{AB} \leq 24.0$) are taken into account. The median redshifts of the distributions down to $K_{Vega} \leq 20.5$ closely approach those of the whole VVDS samples both for secure and less secure redshifts (see values quoted in Fig. 7). The K-magnitude distribution of the spectroscopic sample is shown in Fig. 6. The distributions for both the pure K-selection and the combined K/I_{AB}-selection are displayed.

A slight incompleteness in colour is present at faint K-band magnitudes to the completeness limit of our survey because of the $I_{AB} \leq 24$ mag limit of the VVDS specroscopic survey, that tends to discourage faint red objects. The effect of the spectroscopic I_{AB} magnitude limit is illustrated in Fig. 8, where it is shown that, for $K_{Vega} > 19.0$, the spectroscopic survey starts missing some objects with red $I - K$ colours. Objects with $I_{AB} > 24$ represent an increasing fraction of progressively bluer sources for increasingly faint K magnitudes. As a result, a ~10% (13%) colour incompleteness arises in the 0.5 mag bin centred at $K_{Vega} = 19.75$ (20.25). However, photometric redshifts can be used to circumvent this problem.

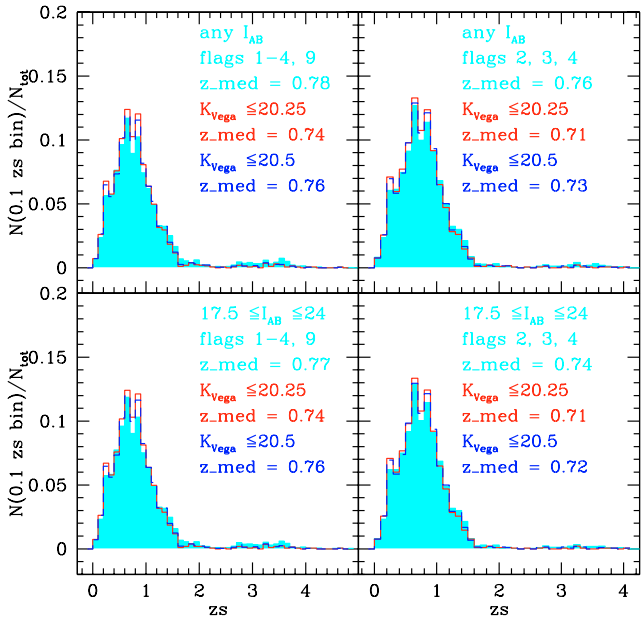

Fig. 7. Normalised redshift distribution of the K-selected spectroscopic sample (including only sources spectroscopically classified as galaxies) down to $K_{Vega} \leq 20.25$ (red empty histogram) and to $K_{Vega} \leq 20.5$ (dashed blue line) compared to the one of the entire VVDS sample within the same sky area (cyan filled histogram). The left-hand panels include flags 1−4, 9, and their equivalents, whereas the right-hand panels include only secure redshifts with flags 2−4, 9 and their equivalents. The top panels show the redshift distribution irrespective of the I-magnitude values (i.e. including secondary objects falling outside the selection criteria of the spectroscopic survey), whereas the bottom panels show only the objects within the VVDS magnitude selection limits. The median redshifts z_{med} of the distributions are quoted.

4. Photometric redshifts

The photometric redshifts for our K-selected sources were obtained with the code Le_Phare[5] (developed by S. Arnouts and O. Ilbert), by following the procedure described in Ilbert et al. (2006) and using MAG_AUTO magnitudes[6] measured in the maximum number of available photometric bands in the set $u^*g'r'i'z'BVRIJK$. The J-band magnitudes (or upper limits) are available only for a sub-area of ~160 arcmin^2, i.e. for 26% of the objects in our K-band catalogue. In all our photometric redshift determinations we applied the corrections for systematic offsets of the zero-points and the optimised galaxy templates described in detail in Ilbert et al. (2006).

As shown by Ilbert et al. (2006), a Bayesian approach (Benítez 2000) with the introduction of an a priori information

[5] http://www.lam.oamp.fr/arnouts/LE_PHARE.html

[6] Magnitudes were measured in all bands with SExtractor in double-image mode, by using the χ^2 image as detection image.

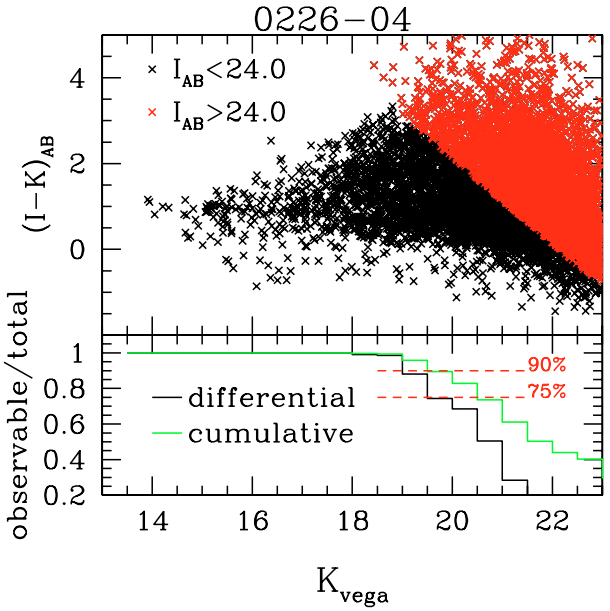

Fig. 8. The $I - K$ vs. K magnitude diagram for sources with $I_{AB} < 24$ (black) and $I_{AB} > 24$ (red) and the differential (black), and cumulative (green) distributions of K magnitudes illustrate the effects of the I_{AB} magnitude cut of the spectroscopic survey on the completeness of the K-selected spectroscopic sample. A slight colour incompleteness arises in the last two 0.5 mag bins down to $K_{Vega} \leq 20.5$.

on the redshift probability distribution function significantly improves the determination of photometric redshifts with respect to the traditional χ^2 method. In this work, consistently with Ilbert et al. (2006) and supported by the similarity shown in Fig. 7 between $K < 20.5$ and VVDS redshift distributions, we directly use a prior based on the second one and we compare the results obtained with/without the application of this prior to those obtained with/without the use of the K-band photometry in addition to the other bands during the fitting procedure with Le_Phare. This exercise allows us to determine the influence of the K-band on the quality of the photometric redshifts. In comparing the photometric redshifts (zp) with the spectroscopic ones (zs), we express the redshift accuracy in terms of $\sigma_{\Delta z/(1+zs)}$ using the normalised median absolute deviation defined as $1.48 \times \text{median}(|\Delta z|/(1 + zs))$, while for the catastrophic errors we adopt the definition $|zs - zp|/(1 + zs) > 0.15$. In analogy to Ilbert et al. (2006), we split our K-selected spectroscopic sample into an i'-bright ($17.5 \leq i' \leq 22.5$) and an i'-faint ($22.5 < i' \leq 24.0$) subsample to check the quality of the photometric redshifts. Also, we applied our test down to three different limits in K magnitude ($K_{Vega} \leq 20.25, 20.5, 21.5$), to evaluate the effects of including K-faint sources. To ensure the use of reliable photometric redshifts, we considered only those based on ≥5 photometric bands (including the K band). Moreover, to avoid side-effects related to the quality of spectroscopic redshifts, we limited the comparison to galaxies with spectroscopic flags 3, 4, 23, and 24, although we recognise that this choice could bias our subsamples toward classes of objects whose spectral properties favour the redshift measurement. The results are summarized in Table 4, where we report the values of $\sigma_{\Delta z/(1+zs)}$ and the fraction of catastrophic errors η for the selected subsamples of galaxies and the total number of objects we used for our test.

Figure 9 illustrates the effects of including the K-band and the prior on the quality of photometric redshifts for the K-selected spectroscopic sample down to $K_{Vega} \leq 20.25$ (the results for the samples down to fainter K magnitude limits are alike). It is evident that including the K-band, even without the use of any prior, is more effective than using the prior alone for reducing the number of catastrophic redshifts, especially for objects that are erroneously assigned a photometric redshift in the range $2 < zp \leq 3.5$. The best result is obtained with the use of both the K-band and the prior, which gives $\sigma_{\Delta z/(1+zs)} = 0.026$ and $\eta = 1.61\%$ for the i'-bright subsample, and $\sigma_{\Delta z/(1+zs)} = 0.028$ and $\eta = 2.43\%$ for the entire sample, at least in the covered redshift range.

Objects spectroscopically classified as active galactic nuclei are not considered in the comparison shown here. Their inclusion would increment the catastrophic errors, but would leave the outcome of the comparison unchanged, with the best quality of photometric redshifts achieved by including both the K-band and the prior in the fitting process.

Because of the $I_{AB} \leq 24$ mag limit of the sample upon which the prior is based, we decided to adopt photometric redshifts determined without the prior for sources fainter than this limit. In Fig. 10 we show the photometric redshift distribution of our sample, after excluding candidate stars, identified as described in Sect. 5. The redshift distribution is shown for the two magnitude limits $K_{Vega} \leq 20.25$ and $K_{Vega} \leq 20.5$ for a purely K-selected sample and for a sample with an additional I-selection that reproduces the magnitude limits of the VVDS spectroscopic survey. The effect of the additional I-selection is the loss of objects especially at intermediate to high redshift and, therefore, a lowering of the median redshift of the sample. The median redshift of the purely K-selected photometric sample down to $K_{Vega} \leq 20.25$ (20.5) is $zp_{med} = 0.87$ (0.91).

The photometric redshifts determined in this work are used in a companion paper that is dedicated to K-selected extremely red objects (Temporin et al. 2008) extracted from our K-band wide catalogue.

5. Star-galaxy separation

We classified point-like objects with a combination of photometric and morphological criteria, using parameters derived by SExtractor and Le_Phare. We adopted a complex strategy since our aim is to perform the star/galaxy separation even at faint magnitudes, where most of the single criteria are known to fail.

The chosen parameters and adopted criteria are the following:

i) the CLASS_STAR parameter given by SExtractor, providing the "stellarity-index" for each object; selected point-like sources obey CLASS_STAR ≥ 0.95, 0.90 for objects brighter/fainter then $i'_{AB} < 22.5$;
ii) the FLUX_RADIUS parameter, also computed by SExstractor in the K-band and denoted as $r_{1/2}$, measuring the radius that encloses 50% of the object total flux; we imposed $r_{1/2} < 3.4$ pixels as the criterion to be satisfied by stellar sources;
iii) the MU_MAX parameter by SExtractor, representing the peak surface brightness above the background; the locus of selection of stellar objects in the i' vs. MU_MAX plot was derived empirically using the spectroscopic sample;
iv) the BzK criterion, proposed by Daddi et al. (2004), with stars characterised by colours $z - K < 0.3(B - z) - 0.5$;
v) the χ^2 and of the SED fitting carried out with Le_Phare during the photometric redshift estimate, by using template

Table 4. Quality of photometric redshifts determined with/without K-band photometry and with/without prior down to different K magnitude limits and for two intervals of i' magnitudes.

	$K \leq 20.25$	$K \leq 20.5$	$K \leq 21.5$	$K \leq 20.25$	$K \leq 20.5$	$K \leq 21.5$
Nobj	890	917	946	347	453	817
	$17.5 \leq i' \leq 22.5$			$22.5 < i' \leq 24.0$		
	without K, without prior					
$\sigma_{\Delta z/(1+z)}$	0.0280	0.0280	0.0280	0.0384	0.0379	0.0351
η (%)	7.75	8.18	8.35	7.78	7.73	7.71
	with K, without prior					
$\sigma_{\Delta z/(1+z)}$	0.0265	0.0265	0.0267	0.0349	0.0345	0.0327
η (%)	1.91	1.96	2.11	5.76	5.30	5.38
	without K, with prior					
$\sigma_{\Delta z/(1+z)}$	0.0270	0.0268	0.0268	0.0381	0.0367	0.0339
η (%)	2.58	2.62	2.85	6.05	5.52	5.88
	with K, with prior					
$\sigma_{\Delta z/(1+z)}$	0.0264	0.0264	0.0265	0.0350	0.0336	0.0322
η (%)	1.69	1.75	1.90	4.32	3.97	4.65

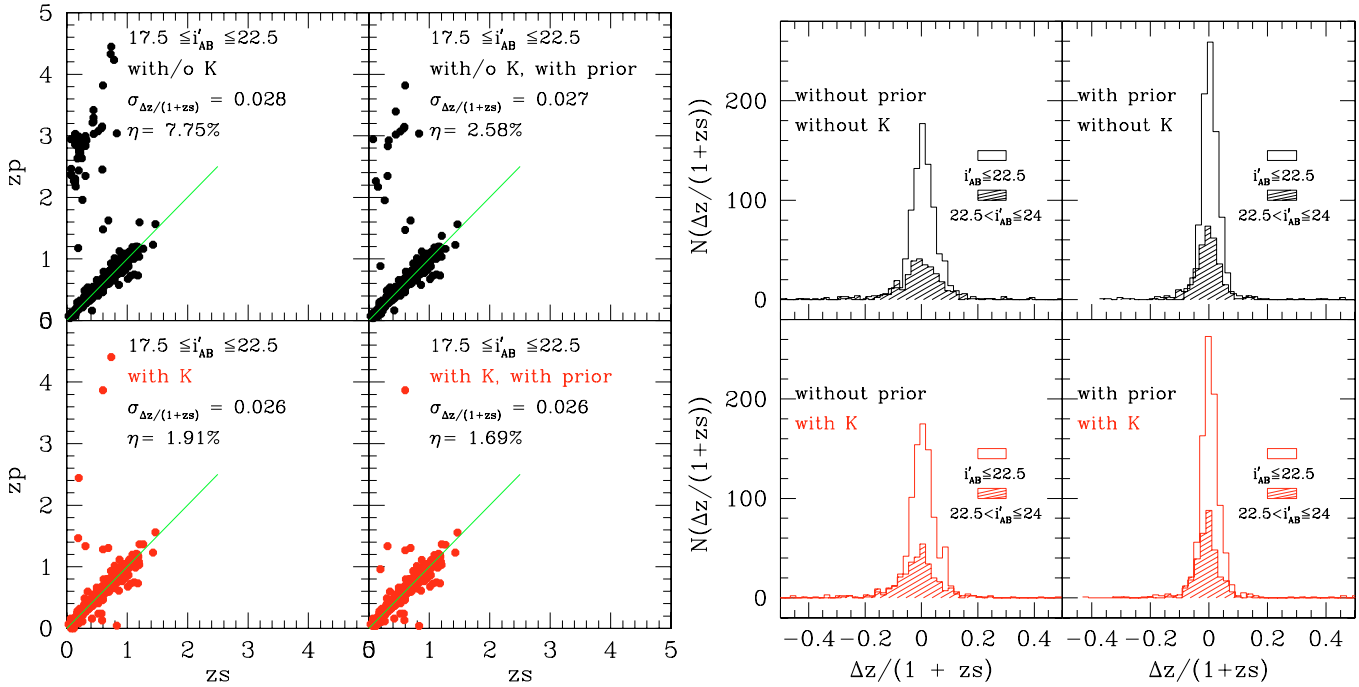

Fig. 9. Comparison between spectroscopic and photometric redshifts for the i'-bright subsample (*left-hand panels*) and distribution of $\Delta z/(1+zs)$ for the i'-bright and i'-faint subsamples (*right-hand panels*, empty and shaded histograms, respectively). See text for details. The $zp = zs$ line is displayed in green. The results for Le_Phare fits with/without prior and with/without including K-band photometry are shown with the relevant values of $\sigma_{\Delta z/(1+zs)}$ and η. The results for the fits with the K-band are displayed in red.

SEDs of both stars ($\chi^2_{\rm star}$)and galaxies ($\chi^2_{\rm gal}$); the criterion to be satisfied by a stellar source is $\chi^2_{\rm gal} - \chi^2_{\rm star} > 0$.

The application of the above criteria to the spectroscopic sample is shown in Fig. 11. Objects fulfilling at least 4 of the above-mentioned criteria have been classified as point-like, whereas a less restrictive constraint has been imposed for objects brighter than $K_{\rm Vega} = 17.16$, with only 3 out of 5 criteria fulfilled. Moreover, to be certain not to miss stellar saturated objects, we included in the point-like objects selection all the sources with $r_{1/2} < 4$ and $K_{\rm Vega} < 14.16$ ignoring the other criteria.

The selection yields 745 point-like objects at $K_{\rm Vega} \leq 20.5$, with 235 of them belonging to the spectroscopic sample. Within this subsample, 80% of the spectroscopic stars are correctly identified and only 3 spectroscopic galaxies and 4 active galactic nuclei with very reliable redshift (flag = 3, 4, 13, 14) fall into the star candidate subsample. The galaxy sample is found to be contaminated by misclassified stars at the 2% level.

This method for the star-galaxy separation represents an improvement over both the method used by Ilbert et al. (2006) and the one adopted by Pozzetti et al. (2007), as we verified on the spectroscopic sample.

Our final classification of the objects takes the spectroscopic information into account when this is flagged as highly reliable (flag = 3, 4, 23, 24, 13, 14, 213, 214) by overriding the photometric classification with the spectroscopic one.

6. Galaxy and star number counts

Comparing number counts of galaxies and stars with published compilations is a good check both of the star-galaxy separation efficiency and of the reliability of our photometry, as well as

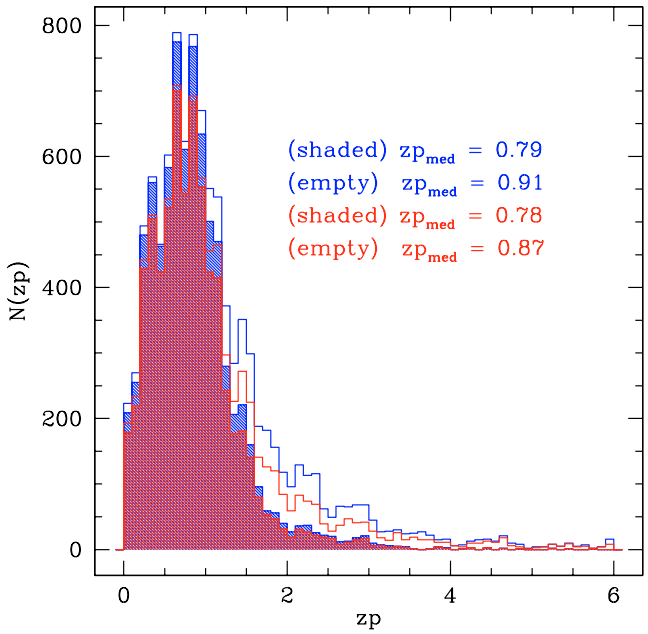

Fig. 10. Distribution of photometric redshifts for the K-selected photometric samples down to $K_{\rm Vega} \leq 20.25$ (red) and $K_{\rm Vega} \leq 20.5$ (blue). Shaded histograms show the redshift distribution when an additional I-selection matching the VVDS selection for the spectroscopic survey is applied. The median photometric redshifts of each distribution are reported.

the sample reliability and completeness. The differential number counts of stars (number 0.5 mag^{-1} deg^{-2}) for the F02 wide field are shown in Fig. 12. To avoid underestimating bright-star counts, for this exercise we used the catalogues before excising the areas around bright stars. The continuous line is the prediction of the model of Robin et al. (2003) computed at the appropriate galactic latitude. The agreement between observed and predicted star counts is very good (the error bars shown are Poissonian error bars), confirming the reliability both of our photometry and of our star-galaxy separation procedure.

Figure 13 shows the differential number counts (number (0.5 mag)$^{-1}$ deg^{-2}) for the F02 wide field. The observed raw number counts were normalised to the total field after excising areas around bright stars (616 arcmin^2). The error bars shown are Poissonian error bars, and no correction for stellar contamination has been applied to the raw counts shown. The contamination estimated from the prediction of the model of Robin et al. (2003) is below 3% for the fainter bins shown in the plot. Also shown are the total galaxy counts obtained after correcting the counts for stellar contamination estimated using our star-galaxy separation. We did not apply any further completeness or contamination correction to our data, because such corrections are negligible down to the limiting magnitude ($K_{\rm Vega} = 20.5$) plotted in Fig. 13.

Table 5 lists our raw differential number counts per half magnitude bin, the total raw number densities in units of number (0.5 mag)$^{-1}$ deg^{-2}, and the final, corrected for stellar contamination, differential galaxy densities, together with their Poissonian 1σ error bars.

Figure 14 shows our total corrected galaxy counts compared with a selection of literature data. We followed the approach of Cristóbal-Hornillos et al. (2003) and selected only reliable counts data from the literature, considering only data with negligible incompleteness correction and with the star-galaxy separation applied. We were conservative in the selection of the magnitude intervals plotted in our counts, restricting ourselves to bins with a relatively large number of galaxies, negligible incompleteness, and small contamination corrections. The agreement with literature data is very good. Our F02 wide galaxy counts confirm the change of slope around $K_{\rm Vega} \sim 18.0$ previously detected by Iovino et al. (2005), Gardner et al. (1993) and Cristóbal-Hornillos et al. (2003). In the range $18 < K_{\rm Vega} < 20.5$ the slope of the galaxy counts is $\gamma_K \sim 0.30 \pm 0.09$, while in the brighter magnitude range, $15.0 < K_{\rm Vega} < 18.0$, the slope is steeper: $\gamma_K \sim 0.42 \pm 0.02$.

7. Clustering analysis for K-selected data

In this section we investigate the clustering properties of point-like and extended sources in the F02 wide K-band catalogues.

We use the projected two-point angular correlation function, $\omega(\theta)$, which measures the excess of pairs separated by an angle $\theta, \theta + \delta\theta$ with respect to a random distribution. This statistic is useful for our purposes because it is particularly sensitive to any residual variations in the magnitude zero-point across our stacked images. We measure $\omega(\theta)$ using the standard Landy & Szalay (1993) estimator, i.e.,

$$\omega_{\rm e}(\theta) = \frac{\rm DD - 2DR + RR}{\rm RR}, \quad (1)$$

with the DD, DR and RR terms referring to the number of data-data, data-random and random-random pairs between θ and $\theta + \delta\theta$. We use logarithmically spaced bins, with $\Delta \log(\theta) = 0.2$, and the angles are expressed in degrees, unless stated otherwise. DR and RR are obtained by populating the two-dimensional coordinate space corresponding to the different fields' number of random points equal to the number of data points, a process repeated 1000 times to obtain stable mean values of these two quantities.

7.1. Clustering of point-like sources

We first measure the angular correlation function $\omega(\theta)$ of the stellar sources. As stars are unclustered, we expect that, if our magnitude zero-points and detection thresholds are uniform over our field, then $\omega(\theta)$ should be zero at all angular scales.

The results for F02 wide-field K-band data are displayed in Fig. 15, where the correlation function is plotted for the total sample of stars obtained from our wide field according to the procedure described in Sect. 5: 617 stars in the K-band interval $15.00 \leq K \leq 20.25$. On all scales displayed, the measured correlation values are consistent with zero. Error bars are obtained through bootstrap resampling of the star sample (and are roughly twice Poissonian error bars).

7.2. Clustering of extended sources

The procedure followed to measure $\omega(\theta)$ is similar to the one described above for the star sample. In the case of galaxies, a positive amplitude of $\omega(\theta)$ is expected, and we have to take into account the so-called "integral constraint" bias. If the real $\omega(\theta)$ is assumed to have the form $A_\omega \theta^\delta$, our estimator (1) will be offset negatively from the true $\omega(\theta)$, according to the formula:

$$\omega_{\rm e}(\theta) = A_\omega(\theta^{-\delta} - C). \quad (2)$$

This bias increases as the area of observation decreases, and it is caused by the need to use the observed sample itself to estimate

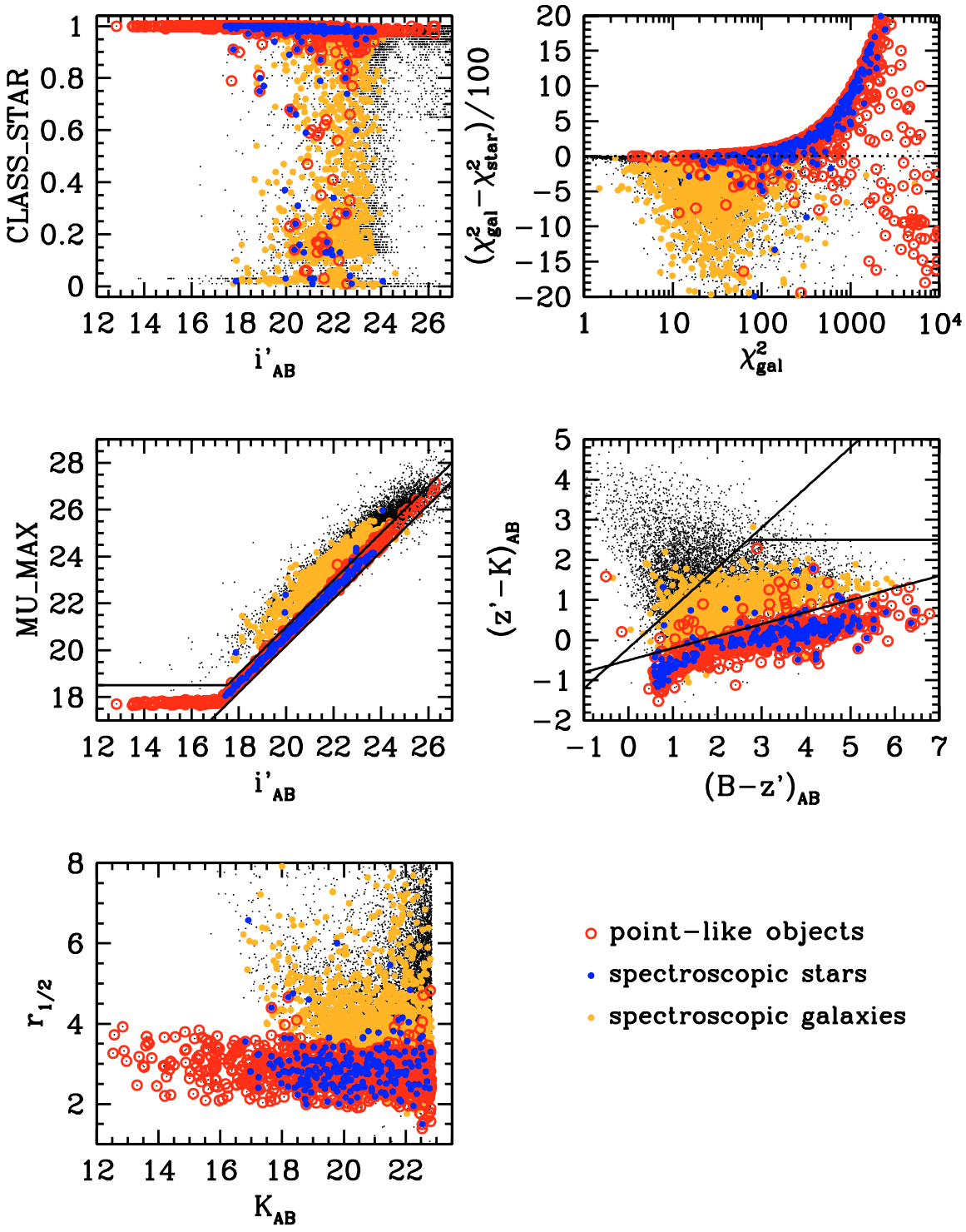

Fig. 11. The five criteria for the star-galaxy separation (see text) applied to the spectroscopic sample. *From top to bottom, and left to right*, the SExtractor CLASS_STAR, MU_MAX, and FLUX_RADIUS parameters, the Le_Phare best-fit χ^2 values, and the *BzK* diagram (Daddi et al. 2004) are plotted. Each panel illustrates an individual photometric criterion and the corresponding candidate stellar sources (red circles), overplotted to spectroscopically classified galaxies (yellow dots) and stars (blue dots).

its mean density, see e.g. Peebles (1980). The negative offset AC can be estimated by doubly integrating the assumed true $\omega(\theta)$ over the field area Ω:

$$A_\omega C = \frac{1}{\Omega^2} \int\int \omega(\theta) \mathrm{d}\Omega_1 \mathrm{d}\Omega_2. \quad (3)$$

This integral can be solved numerically using randomly distributed points for each field:

$$C = \frac{\sum N_{rr}(\theta)\, \theta^{-\delta}}{\sum N_{rr}(\theta)}\,. \quad (4)$$

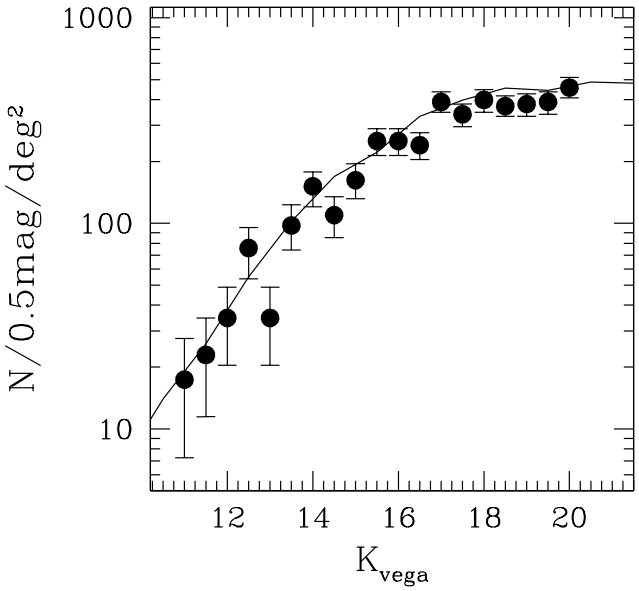

Fig. 12. Differential number counts of stars in the F02 wide field. The continuous lines are the prediction of the model of Robin et al. (2003).

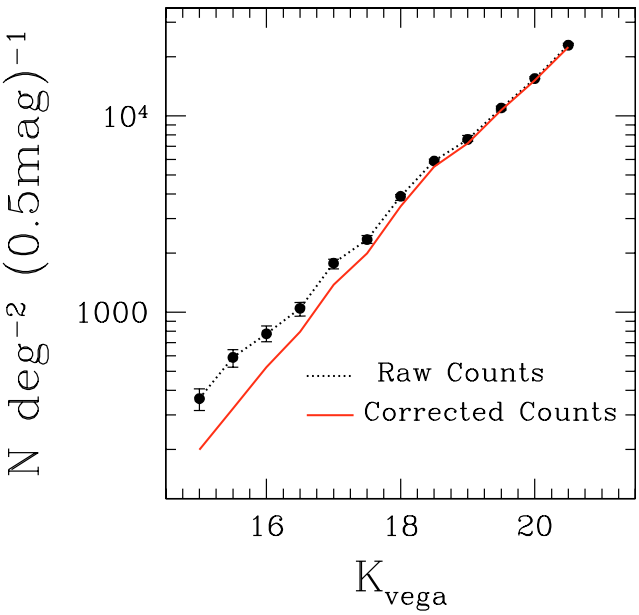

Fig. 13. Differential K-band number counts in the F02 wide field. The dotted line shows the raw number densities and error bars are Poissonian. The heavy line shows galaxy densities obtained after correcting for star contamination.

Assuming 1″ as the pairs' minimal scale at which two galaxies can be distinguished as separated objects, and $\delta = 0.8$, we obtain the following value: $C_{\rm Wide} = 4.50$.

We estimated the amplitude A_ω for a series of K-limited galaxy samples by least-square fitting $A(\theta^{-0.8} - C)$ to the observed $\omega(\theta)$, weighting each point using bootstrap error bars. Figure 16 shows the results obtained for 6 different K-band limiting magnitudes. No correction for stellar contamination is applied (only the objects classified as stars, using the method described in Sect. 5, were excluded from the analysis) and the error bars on the amplitude are those from the fit.

Figure 17 shows the comparison of our results with literature data and the models of PLE from Roche et al. (1998), with

Table 5. Raw, differential number counts and galaxy densities.

$K_{\rm vega}$	total counts[a]	$N_{\rm raw}$ 0.5 mag^{-1} deg^{-2}	$N_{\rm corr}$ 0.5 mag^{-1} deg^{-2}	σ
15	62	363	199	34
15.5	100	585	322	43
16	133	778	520	55
16.5	178	1041	801	68
17	302	1766	1374	90
17.5	402	2351	2006	108
18	660	3859	3462	142
18.5	1007	5889	5514	180
19	1309	7655	7275	206
19.5	1881	10 999	10 614	249
20	2671	15 619	15 157	298

[a] Column 2 lists the raw, differential number counts per half magnitude bin. Raw number densities and differential galaxy densities after correction for star contamination are given in Cols. 3 and 4, and their 1σ error bar in Col. 5.

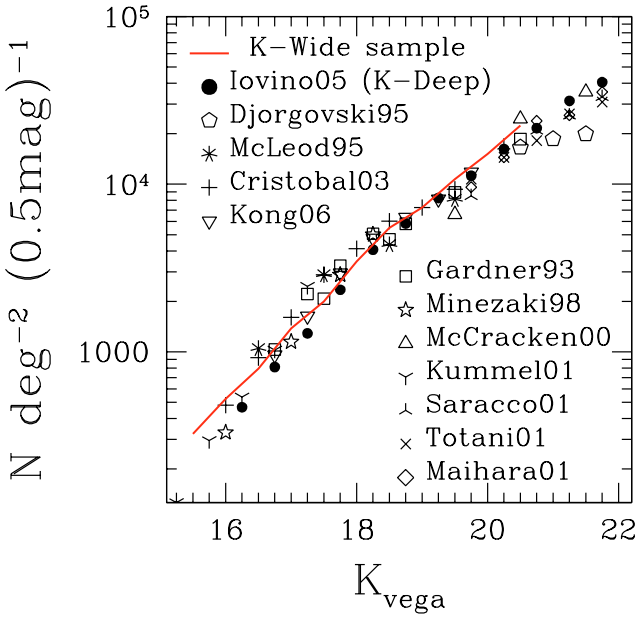

Fig. 14. The K-band galaxy number counts, in units of number 0.5 mag^{-1} deg^{-2}, obtained in this paper compared to a compilation of those from the literature, including counts from Gardner et al. (1993), Djorgovski et al. (1995), McLeod et al. (1995), Minezaki et al. (1998), McCracken et al. (2000), Kümmel & Wagner (2001), Saracco et al. (2001), Totani et al. (2001), Maihara et al. (2001), Cristóbal-Hornillos et al. (2003), Iovino et al. (2005), and Kong et al. (2006).

scaling from local galaxy clustering. Table 6 lists our amplitude measurements for the F02 sample, in units of 10^{-4} at 1 deg, together with their bootstrap 1σ error bars. For each K-band limiting magnitude, the total number of objects N used in the analysis is also listed.

8. Conclusions

We have presented a new K-band catalogue that covers a contiguous sky area of 623 arcmin^2 down to a magnitude limit $K_{\rm Vega} \leq 21.5$ and provides us with a 90% complete K-selected sample down to $K_{\rm Vega} \leq 20.5$, although with some possible level of colour incompleteness potentially affecting extremely red sources fainter than $K_{\rm Vega} = 20.5$, whose inclusion is discouraged by the procedure of building the catalogue at these

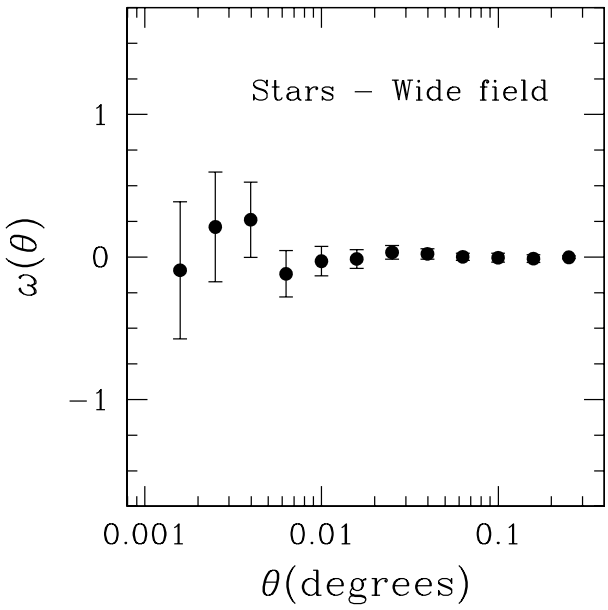

Fig. 15. Plot of the correlation function $\omega(\theta)$ for the total sample of stars in the K-band stacks as a function of the logarithm of the angular pair separation in degrees. On all the scales displayed, the measured correlation values are consistent with zero.

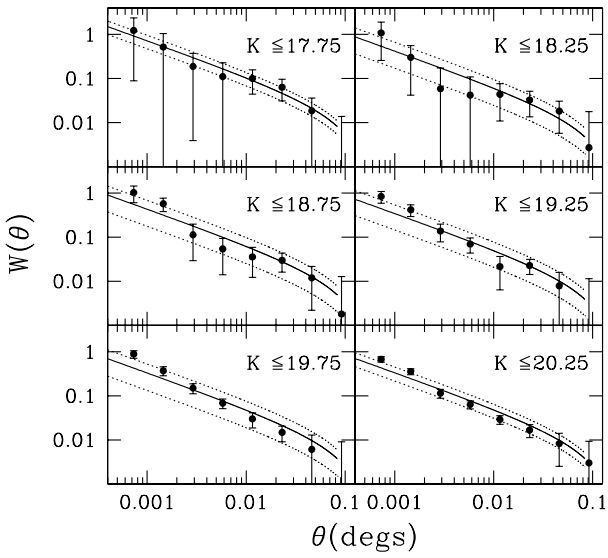

Fig. 16. Results for the amplitude A_ω at 1 deg of our F02 wide field on galaxy sub-samples of different K-band limiting magnitudes. No correction for stellar contamination is applied and the error bars on the amplitude are those obtained from the fit.

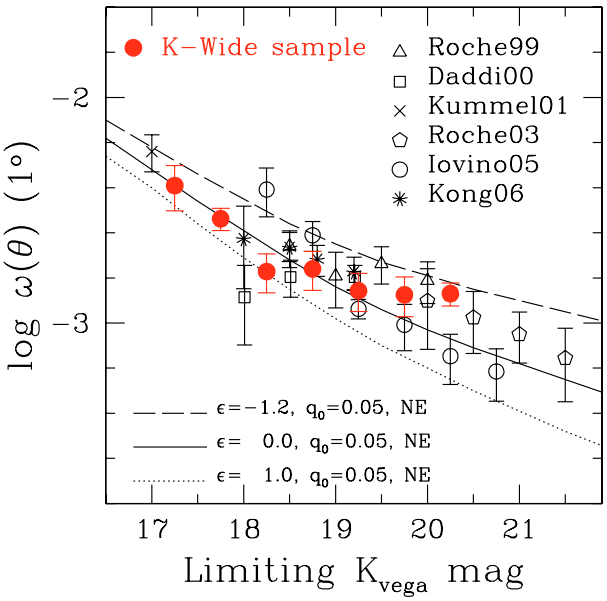

Fig. 17. Our total sample estimate of the amplitude, A_ω at 1 deg, of the angular correlation function compared with a compilation of results from the literature in similar magnitude ranges. We include mesurements from: Roche et al. (1999), Daddi et al. (2000), Kümmel & Wagner (2001), Roche et al. (2003), Iovino et al. (2005), and Kong et al. (2006). The continuous, dotted and dashed lines show, for reference, the models of PLE from Roche et al. (1998), with scaling from local galaxy clustering.

Table 6. Observed $\omega(\theta)$ amplitudes A for our F02 wide field.

Magnitude	0226-04 (F02)	
	N	$A \pm dA$
$K < 17.25$	561	40.68 ± 9.24
$K < 17.75$	902	28.97 ± 3.25
$K < 18.25$	1486	16.92 ± 3.32
$K < 18.75$	2427	17.39 ± 3.41
$K < 19.25$	3661	13.91 ± 2.67
$K < 19.75$	5470	13.33 ± 2.66
$K < 20.25$	8059	13.49 ± 1.57

faint magnitudes (see discussion in Sect. 3.2). This is one of the biggest K-selected samples available to date at this magnitude limit, and it is complemented by $UBVRIu^*g'r'i'z'$ photometry – available through the VVDS and CFHTLS surveys – as well as by VVDS spectroscopy with a sampling rate of ∼27%, down to the 90% completeness limit.

Good quality photometric redshifts were obtained for the whole sample by following the method outlined by Ilbert et al. (2006) and including the K-band photometry in the fits of the galaxy SEDs. By using our spectroscopic subsample, we explored the effects of including K-band photometry in the determination of photometric redshifts. We verified that the use of the K band leads to similar advantages as provided by the training on the spectroscopic redshift distribution function, namely a considerable reduction of the fraction of catastrophic errors. When no a priori spectroscopic information is adopted to train the fitting procedure, the additional use of the K band improves the determination of photometric redshifts significantly, as expected. The results from this survey show that we expect a significant improvement in the accuracy of photometric redshifts obtained by future wide-field surveys using near-infrared data (e.g. the Visible and Infrared Survey Telescope for Astronomy, VISTA[7]).

Also, taking advantage of the K-band photometric parameters, we implemented quite a complex set of criteria for the star-galaxy separation that improved on methods previously adopted by our team (Ilbert et al. 2006; Pozzetti et al. 2007). A very good agreement of star and galaxy number counts with those present in the literature has proven the effectiveness of our star-galaxy separation method, as well as the good quality of our photometry and the reliability and completeness of our sample.

The good quality of our photometry, as well as the reliability and completeness of the sample, are confirmed by comparison of the number counts of stars and galaxies with published

[7] http://www.vista.ac.uk

compilations. The K-band galaxy number counts from this work are in excellent agreement with those obtained from the K-deep sample (Iovino et al. 2005) and with a selection of compilations from the literature. The projected two-point angular correlation function does not show any peculiarity as a function of magnitude and angular scale and it broadly agrees with results from the literature.

The galaxy mass function, the luminosity function, and the properties of extremely red objects based on our K-selected catalogue are presented in companion papers (Pozzetti et al. 2007; Bolzonella et al. 2008; Temporin et al. 2008; Bondi et al. 2008). A cross-match of this K-band catalogue with radio sources from the VVDS-VLA deep field was carried out by Bondi et al. (2007) and has revealed a higher incidence of faint K-band counterparts ($K_{\rm Vega} > 20$) among candidate ultra-steep-spectrum radio sources compared to the rest of the radio sources in the sample, although based on small number statistics.

Acknowledgements. This research was developed within the framework of the VVDS consortium. We are grateful to E. Pompei who provided us with the additional NTT K-band observations needed to complete a pointing, in February 2006. We thank the anonymous referee for his/her constructive comments that helped to make the paper clearer. This work has been partially supported by the CNRS-INSU and its Programme National de Cosmologie (France), and by Italian Ministry (MIUR) grants COFIN2000 (MM02037133) and COFIN2003 (no.2003020150). The VLT-VIMOS observations were carried out on guaranteed time (GTO) allocated by the European Southern Observatory (ESO) to the VIRMOS consortium, under a contractual agreement between the Centre National de la Recherche Scientifique of France, heading a consortium of French and Italian institutes, and ESO, to design, manufacture, and test the VIMOS instrument.

References

Benítez, N. 2000, ApJ, 536, 571
Bertin, E., & Arnouts, S. 1996 A&AS, 117, 393
Bertin, E., Mellier, Y., Radovich, M., et al. 2002, ASP Conf. Ser., 281, 228
Bolzonella, M., et al. 2008, in preparation
Bondi, M., Ciliegi, P., Zamorani, G., et al. 2003, A&A, 403, 857
Bondi, M., Ciliegi, P., Venturi, T., et al. 2007, A&A, 463, 519
Bondi, M., et al. 2008, in preparation
Cimatti, A., Pozzetti, L., Mignoli, M., et al. 2002, A&A, 391, L1
Coleman, G. D., Wu, C.-C., & Weedman, D. W. 1980, ApJS, 43, 393
Conselice, C. J., Bundy, K., Trujillo, I., et al. 2007, MNRAS, in press [arXiv:0708.1040v1]
Cristóbal-Hornillos, D., Balcells, M., Prieto, M., et al. 2003, ApJ, 595, 71
Daddi, E., Cimatti, A., Pozzetti, L., et al. 2000, A&A, 361, 535
Daddi, E., Cimatti, A., Renzini, A., et al. 2004, ApJ, 617, 746
Djorgovski, S., Soifer, B. T., Pahre, M. A., et al. 1995, ApJ, 438, L13
Drory, N., Feulner, G., Bender, R., et al. 2001, MNRAS, 325, 550
Dye, S., Warren, S. J., Hambly, N. C., et al. 2006, MNRAS, 372, 1227
Förster Schreiber, N. M., Franx, M., Labbé, I., et al. 2006, AJ, 131, 1891
Gardner, J. P., Sharples, R. M., Carrasco, B. E., & Frenk, C. S. 1996, MNRAS, 282, L1
Ilbert, O., Arnouts, S., McCracken, H. J., et al. 2006, A&A, 457, 841
Iovino, A., McCracken, H. J., Garilli, B., et al. 2005, A&A, 442, 423
Kong, X., Daddi, E., Arimoto, N., et al. 2006, ApJ, 638, 72
Kümmel, M. W., & Wagner, S. J. 2001, A&A, 370, 384
Labbé, I., Franx, M., Rudnick, G., et al. 2003, AJ, 125, 1107
Landy, S. D., & Szalay, A. S. 1993, ApJ, 412, 64
Le Brun, V., Moreau, C., Garilli, B., et al. 2007, A&A, submitted
Le Févre, O., Vettolani, G., Garilli, B., et al. 2005, A&A, 439, 845
Maihara, T., Iwamuro, F., Tanabe, H., et al. 2001, PASJ, 53, 25
McCracken, H. J., Metcalfe, N., Shanks, T., et al. 2000, MNRAS, 311, 707
McCracken, H. J., Radovich, M., Bertin, E., et al. 2003, A&A, 410, 17
McLeod, B. A., Bernstein, G. M., Rieke, M. J., Tollestrup, E. V., & Fazio, G. G. 1995, ApJS, 96, 117
Minezaki, T., Kobayashi, Y., Yoshii, Y., & Peterson, B. A. 1998, ApJ, 494, 111
Monet, D. G. 1998, BAAS, 30, 1427
Moorwood, A., Cuby, J.-G., & Lidman, C. 1998, The Messenger, 91, 9
Peebles, P. J. E. 1980, The large-scale structure of the universe (Research supported by the National Science Foundation) (Princeton, N. J.: Princeton University Press), 435
Persson, S. E., Murphy, D. C., Krzeminski, W., Roth, M., & Rieke, M. J. 1998, AJ, 116, 2475
Pozzetti, L., Bolzonella, M., Lamareille, F., et al. 2007, A&A, 474, 443
Quadri, R., Marchesini, D., van Dokkum, P., et al. 2007, AJ, 134, 1103
Radovich, M., Arnaboldi, M., Ripepi, V., et al. 2004, A&A, 417, 51
Robin, A. C., Reylé, C., Derrière, S., & Picaud, S. 2003, A&A, 409, 523
Roche, N., Eales, S., & Hippelein, H. 1998, MNRAS, 295, 946
Roche, N., Eales, S. A., Hippelein, H., & Willott, C. J. 1999, MNRAS, 306, 538
Roche, N. D., Dunlop, J., & Almaini, O. 2003, MNRAS, 346, 803
Sabbey, C. N., McMahon, R. G., Lewis, J. R., & Irwin, M. J. 2001, in Astronomical Data Analysis Software and Systems X, ASP Conf. Ser., 238, 317
Saracco, P., Giallongo, E., Cristiani, S., et al. 2001, A&A, 375, 1
Schlegel, D. J., Finkbeiner, D. P., & Davis, M. 1998, ApJ, 500, 525
Szalay, A. S., Connolly, A. J., & Szokoly, G. P. 1999, AJ, 117, 68
Temporin, S., Iovino, A., McCracken, H. J., et al. 2008, in preparation
Totani, T., Yoshii, Y., Maihara, T., Iwamuro, F., & Motohara, K. 2001, ApJ, 559, 592
Warren, S. J., Hambly, N. C., Almaini, O., et al. 2007, MNRAS, 375, 213

[1] Laboratoire AIM, CEA/DSM – CNRS – Université Paris Diderot, IRFU/SAp, 91191 Gif-sur-Yvette, France
e-mail: sonia.temporin@cea.fr
[2] INAF – Osservatorio Astronomico di Brera, via Brera 28, 20121 Milano, Italy
[3] IASF-INAF, via Bassini 15, 20133 Milano, Italy
[4] INAF – Osservatorio Astronomico di Bologna, via Ranzani 1, 40127 Bologna, Italy
[5] IRA-INAF, via Gobetti 101, 40129 Bologna, Italy
[6] INAF – Osservatorio Astronomico di Capodimonte, via Moiariello 16, 80131 Napoli, Italy
[7] Università di Bologna, Dipartimento di Astronomia, via Ranzani 1, 40127 Bologna, Italy
[8] Laboratoire d'Astrophysique de Toulouse/Tabres (UMR5572), CNRS, Université Paul Sabatier, Toulouse III, Observatoire Midi-Pyrénées, 14 Av. E. Belin, 31400 Toulouse, France
[9] Max Planck Institut fur Astrophysik, 85741 Garching, Germany
[10] Laboratoire d'Astrophysique de Marseille, UMR 6110 CNRS-Université de Provence, BP 8, 13376 Marseille Cedex 12, France
[11] Institut d'Astrophysique de Paris, UMR 7095, 98 bis Bvd Arago, 75014 Paris, France
[12] Observatoire de Paris, LERMA, 61 Avenue de l'Observatoire, 75014 Paris, France
[13] Astrophysical Institute Potsdam, An der Sternwarte 16, 14482 Potsdam, Germany
[14] INAF – Osservatorio Astronomico di Roma, via di Frascati 33, 00040 Monte Porzio Catone, Italy
[15] Universitá di Milano-Bicocca, Dipartimento di Fisica, Piazza delle Scienze 3, 20126 Milano, Italy
[16] Integral Science Data Centre, Ch. d'Écogia 16, 1290 Versoix, Switzerland
[17] Geneva Observatory, Ch. des Maillettes 51, 1290 Sauverny, Switzerland
[18] Astronomical Observatory of the Jagiellonian University, ul Orla 171, 30-244 Kraków, Poland
[19] Centre de Physique Théorique, UMR 6207 CNRS-Université de Provence, 13288 Marseille, France
[20] Centro de Astrofísica da Universidade do Porto, Rua das Estrelas, 4150-762 Porto, Portugal
[21] Institute for Astronomy, 2680 Woodlawn Dr., University of Hawaii, Honolulu, Hawaii 96822, USA
[22] School of Physics & Astronomy, University of Nottingham, University Park, Nottingham, NG72RD, UK